Thickness and Morphology Dependent Electrical Properties of ALD-Synthesized MoS$_2$ FETs

Document status and date:
Published: 01/03/2022

Document Version:
Publisher's PDF, also known as Version of Record (includes final page, issue and volume numbers)

Please check the document version of this publication:

• A submitted manuscript is the version of the article upon submission and before peer-review. There can be important differences between the submitted version and the official published version of record. People interested in the research are advised to contact the author for the final version of the publication, or visit the DOI to the publisher's website.
• The final author version and the galley proof are versions of the publication after peer review.
• The final published version features the final layout of the paper including the volume, issue and page numbers.

Link to publication

Thickness and Morphology Dependent Electrical Properties of ALD-Synthesized MoS$_2$ FETs

Reyhaneh Mahlouji, Marcel A. Verheijen, Yue Zhang, Jan P. Hofmann, Wilhelmus. M. M. (Erwin) Kessels, and Ageeth A. Bol*

MoS$_2$ is a layered 2D semiconductor with thickness-dependent electrical properties. Often, 6–12 nm of MoS$_2$ are advised to be used as the channel material in field-effect transistors (FETs) for achieving an optimal device electrical performance. However, this notion is based on exfoliated MoS$_2$ flakes that cannot be employed for large-area and wafer-scale applications. In this work, the thickness-dependent electrical properties of atomic layer deposition (ALD)-based MoS$_2$ FETs are studied. A two-step approach is used for the synthesis of MoS$_2$, wherein large-area and thickness-controlled MoO$_x$ films are initially grown using plasma-enhanced (PE-)ALD and subsequently sulfurized in H$_2$S gas. The number of MoO$_x$ PE-ALD cycles is varied systematically to obtain MoS$_2$ films with a thickness range of 1–10 nm. Current–voltage (*I–V*) characterization of the fabricated MoS$_2$ FETs with various channel thicknesses reveals that ≈1.2 nm MoS$_2$ suffices in attaining the best device electrical performance. Scanning transmission electron microscopy imaging elucidates that the synthetic MoS$_2$ films are polycrystalline and the resultant ≈1.2 nm of MoS$_2$ are not completely continuous. The empty areas in the polycrystalline MoS$_2$ network can serve as locations for side contact formation, leading to substantial improvements in the device metrics fabricated from such ultrathin MoS$_2$ films.

R. Mahlouji, M. A. Verheijen, W. M. M. Kessels, A. A. Bol
Department of Applied Physics
Eindhoven University of Technology
P.O. Box 513, Eindhoven, MB 5600, The Netherlands
E-mail: a.a.bol@tue.nl
M. A. Verheijen
Eurofins Materials Science
High Tech Campus 11, Eindhoven, AE 5656, The Netherlands
Y. Zhang, J. P. Hofmann
Laboratory of Inorganic Materials and Catalysis
Department of Chemical Engineering and Chemistry
Eindhoven University of Technology
P.O. Box 513, Eindhoven, MB 5600, The Netherlands
J. P. Hofmann
Surface Science Laboratory
Department of Materials and Earth Sciences
Technical University of Darmstadt
Otto-Berndt-Strasse 3, 64287 Darmstadt, Germany

1. Introduction

Over the past decade, layered and 2D transition metal dichalcogenides (TMDCs)[1,2] have drawn significant scientific attention as potential material candidates for next generation of nanoelectronic devices and circuits, beyond complementary metal-oxide-semiconductor.[3–6] Among the 2D TMDCs with semiconducting properties, MoS$_2$ is one of the most extensively studied materials, due to its abundance and its intriguing electronic features.[7,8] Field-effect transistors (FETs) based on MoS$_2$ have showcased unique device figures of merit, namely a high current density (I_{ON}) in the order of 700–1135 μA μm^{-1},[9–11] a low subthreshold swing close to thermionic limits (≈60 mV dec^{-1}),[12,13] a high ON/OFF current ratio in the range of 10^7–10^9,[14–17] high reliability,[16] and low variability.[18] One key feature of MoS$_2$ (and most of the other 2D TMDC semiconductors) is its layer-dependent band structure that enables tuning the electronic properties of this material. For example, bulk MoS$_2$ (more than eight layers) shows an indirect band gap (E_g) of 1.2 eV, whereas a single layer (monolayer) MoS$_2$ exhibits a direct E_g of 1.9 eV.[19–21] Such a dependence on the number of layers has been shown to strongly affect the MoS$_2$ FET device metrics, including its mobility,[22–28] electrical conductivity and conductance,[24,29,30] contact resistance (R_c) as well as the Schottky barrier height (SBH).[31] Based on the experimental evidences, ≈6–12 nm of MoS$_2$ is proposed as the optimal channel thickness to be employed in FETs.[22,23]

To date, the majority of reports covering the thickness dependent MoS$_2$ electrical properties is based on pristine flakes, prepared by mechanical exfoliation (cleavage). Because MoS$_2$ layers are held together by weak interlayer van der Waals (vdW) interactions, multilayers or even a monolayer of MoS$_2$ can be obtained via exfoliation. However, a precise control over the number of MoS$_2$ layers and its ultimate thickness may not be very straightforward using this technique. In addition, exfoliated MoS$_2$ flakes are not suitable for large-area and wafer-scale applications. Therefore, scalable synthesis methods such as metal-organic (MO-) chemical vapor deposition (CVD) have been employed for the preparation of MoS$_2$. These techniques deliver high quality MoS$_2$ films over large areas.[32–37] However, the high thermal budget which is typically used in their processes (high growth temperature and/or long duration) can be

**ADVANCED
SCIENCE NEWS**
www.advancedsciencenews.com

**ADVANCED
ELECTRONIC
MATERIALS**
www.advelectronicmat.de

a concern for the semiconductor industry. In addition, during the (MO-)CVD process, the MoS_2 films are sometimes grown on substrates which are not compatible with conventional technologies (e.g., sapphire). As a result, the as-synthesized MoS_2 films need to be transferred to industry-compatible substrates (e.g., SiO_2/Si). The transfer process can damage MoS_2 or induce undesired contaminations on/into the films.[38,39]

In recent years, atomic layer deposition (ALD) has also received interest for the growth of MoS_2[40–42] and other 2D TMDCs.[43–45] ALD is a transfer-free and low temperature cyclic technique for the deposition of thin films over large areas. This deposition method is based on sequential and self-limiting surface reactions,[46,47] whereby the film composition, thickness, uniformity, and conformality (for high aspect ratio features) can be well controlled. However, the MoS_2 films grown by ALD (or any other synthetic method) unavoidably contain point/line defects, dislocations and vacancy states to some extent.[48–51] Therefore, one primary research question is whether the thickness of synthetic MoS_2 films would influence its electrical properties in a similar way as observed for the exfoliated flakes or not. Earlier reports on synthetic-based MoS_2 films, prepared by CVD[52] or by sulfurizing magnetron sputtered MoO_3,[53] show that the number of MoS_2 monolayers influences its electrical properties. However, a broad range of MoS_2 thicknesses are not covered in these studies.

In this paper, we use a two-step plasma-enhanced (PE-)ALD-based approach for the growth of MoS_2 films, with demonstrated thickness-control down to sub-monolayer regime.[44,45] Initially, series of MoO_x films with a variety of thicknesses are grown using PE-ALD. Then, these films are sulfurized in H_2S gas. Employing this approach improves the crystallization degree of the final MoS_2 films,[45] compared to the direct PE-ALD of MoS_2.[40] In addition, it allows us to still benefit from the ultimate thickness-control feature of PE-ALD in the resultant MoS_2 films, which may not be fully achieved by some other synthesis methods such as CVD. We evaluate the thickness dependence of our MoS_2 film electrical properties through the fabrication and current–voltage (I–V) characterization of back-gate FETs. Furthermore, we investigate the MoS_2 film microstructure, coverage and morphology by top-view scanning transmission electron microscopy (STEM) imaging. Our findings highlight the importance of independently re-evaluating the optimum channel

thickness for the synthetic-based MoS_2 FETs. They also show that the influence of the MoS_2 film morphology on the final device electrical properties should not be underestimated.

2. Results and Discussion

2.1. The As-Synthesized MoS_2 Films

A series of MoO_x films were initially grown by means of PE-ALD at 50 °C and subsequently sulfurized in H_2S gas at 900 °C for 45 min. Using this synthesis approach, monolayers and multilayers of MoS_2 with an interlayer spacing of ≈0.6 nm can be achieved. Details of the MoS_2 film specifications and processing conditions are published in a previous work.[45]

The thicknesses of the initial MoO_x films were controlled by the number of PE-ALD cycles, which were ranging from 10 to 160 cycles. Using in situ spectroscopic ellipsometry (SE), it was found that there is a linear relation between the MoO_x film thickness and the number of PE-ALD cycles (saturated growth). The growth per cycle (GPC) of the MoO_x films was therefore determined to be ≈0.6 Å at 50 °C. Based on this GPC, a MoO_x thickness range of ≈0.6–12.4 nm was obtained for 10–160 PE-ALD number of cycles. After the sulfurization process, the thicknesses of the final MoS_2 films were measured using ex situ SE. A thickness extent of ≈1.2–9.8 nm MoS_2 was obtained for 20–160 PE-ALD cycles of initial MoO_x. Overall, the final MoS_2 films were thinner than the initial MoO_x counterparts. This is most likely due to the MoO_x sublimation[54] that can occur during the sulfurization process at elevated temperatures. A summary of both the MoO_x and MoS_2 thicknesses are provided in Table S1 in the Supporting Information. To validate the SE data for ultrathin films of MoS_2, atomic force microscopy (AFM) line-profiles are measured. The results are shown in Figure S1 in the Supporting Information, revealing that the MoS_2 thickness values obtained from the SE measurements are reasonably in accordance with the AFM measurements.

A general quality inspection of the as-synthesized MoS_2 films was performed using Raman and X-ray photoelectron spectroscopy (XPS). The Raman data are shown in **Figure 1**a for various MoS_2 thicknesses (initial MoO_x number of PE-ALD cycles). The
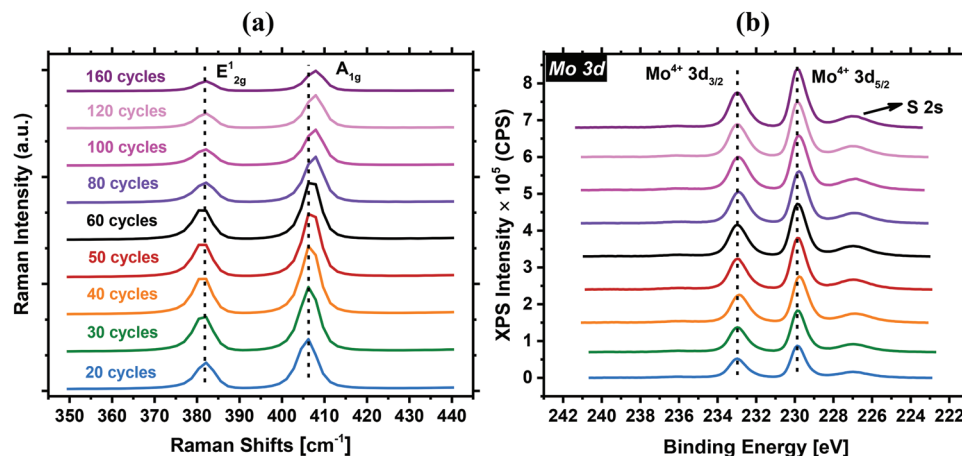

Figure 1. a) The Raman spectra and b) the Mo 3d core level spectra (obtained from the XPS measurements) of the as-synthesized MoS_2 films with various thicknesses (number of initial MoO_x PE-ALD cycles).

measurements clearly confirm the presence of the two characteristic MoS_2 vibrational modes (A_{1g} and E^1_{2g}[55]) even for the ultrathin MoS_2 films. The Mo 3d core level spectrum of the entire MoS_2 thickness series, obtained from the XPS measurements, is also provided in Figure 1b. The peak binding energies were calibrated with respect to the C 1s adventitious carbon peak, set to 284.8 eV. As can be clearly seen, the major Mo 3d doublet peaks (related to the Mo^{4+} oxidation state (MoS_2)) are present for all the studied cases. The Mo $3d_{5/2}$ core level binding energies are in the range of 229.7–229.8 eV and the Mo $3d_{3/2}$ in the range of 232.8–232.9 eV. Signature of the S 2s core level is also discernible at 226.8–226.9 eV. All of these binding energy ranges are in accordance with what is often reported in the literature for the Mo 3d spectrum of MoS_2.[37,51,56] In addition, no significant concentration of the Mo 3d in Mo^{6+} oxidation state is detected, implying that the MoO_x films are efficiently sulfurized upon their exposure to the H_2S gas. For further clarifications, the fitted Mo 3d and O 1s spectra of the 20-, 60- and 160-cycle cases are provided in Figure S2a,b in the Supporting Information. The efficient sulfurization of the MoS_2 films obtained from this approach is also further verified by cross-sectional STEM imaging, provided in a previous work.[45]

2.2. Device I–V Analysis

To evaluate the MoS_2 electrical performance, back-gate FETs with different MoS_2 thicknesses were fabricated and characterized. An optical microscopy image of these devices are shown in **Figure 2**a. In our previous studies, we optimized the Ti/Au contacts[57] and the dielectric capping layer on ≈3.7 nm thick MoS_2 channels (60 cycles of initial MoO_x). Therefore, we consider the devices made from ≈3.7 nm MoS_2 as the reference case throughout our I–V analyses. Furthermore, the MoS_2 films obtained from 10

cycles of initial MoO_x were too resistive and by no means measurable when employed in FETs. As a result, this channel thickness is excluded from our device electrical characterization.

Figure 2b,c shows the transfer curves ($I_{DS}–V_{GS}$) of the fabricated MoS_2 FETs with different channel thicknesses (number of initial MoO_x PE-ALD cycles) in linear and semilog scales, respectively. The data are normalized to the channel width of 1 µm. As can be seen in Figure 2b, the ON-state current (I_{ON}) is the highest for the devices made from 20 and 30 cycles of initial MoO_x. The OFF-state current (I_{OFF}) is better visible in Figure 2c, which is the lowest only for the 15- and 20-cycle cases.

To further elucidate the MoS_2 FET electrical characteristics, statistical measurements were performed on the fabricated devices. **Figure 3**a shows the average I_{ON} as a function of the initial MoO_x PE-ALD number of cycles and MoS_2 thickness. The data are obtained by measuring three-four devices at different locations on each sample. As can be seen from the plot, upon reducing the MoS_2 thickness or the initial MoO_x number of deposition cycles from 60 (reference) down to 15, a nonmonotonic trend is observed. I_{ON} increases at least one order of magnitude and reaches 10.0 µA µm^{-1} for the devices with 30 cycles of initial MoO_x. Then, it drops to 0.5 µA µm^{-1} for the devices with 15 cycles of initial MoO_x. On the other side of the spectrum, thicker MoS_2 channels demonstrate a degraded I_{ON}, as compared with the reference.

The mean maximum field-effect mobility (μ_{FE}) is also provided in Figure 3b. This value can be extracted from the following equation[58]

$$\mu_{FE} = (L/W)(g_m/(C_{ox}V_{DS}))\tag{1}$$

In Equation (1), L and W are the length and width of the channel, g_m is the transconductance, and C_{ox} is the back-oxide

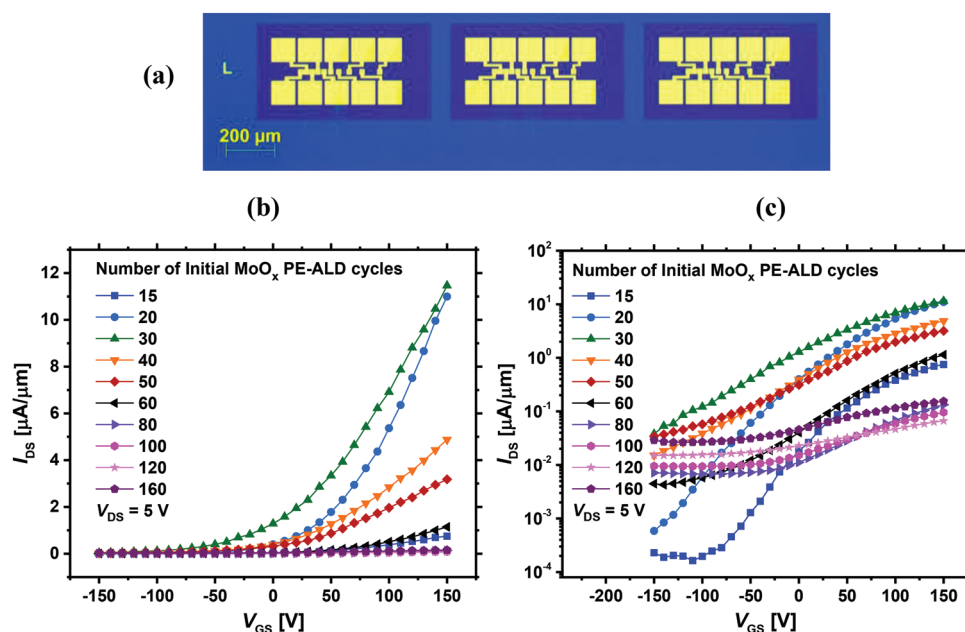**Figure 2.** a) Optical microscopy of the fabricated MoS_2 FETs (yellow regions are the Ti/Au contact pads and dark blue regions are where the MoS_2 is dry-etched), (b) and (c) are the transfer data of the fabricated MoS_2 FETs with various channel thicknesses (number of initial MoO_x PE-ALD cycles) in linear and semilog scales, respectively. Data are normalized with respect to the channel width (1 µm).
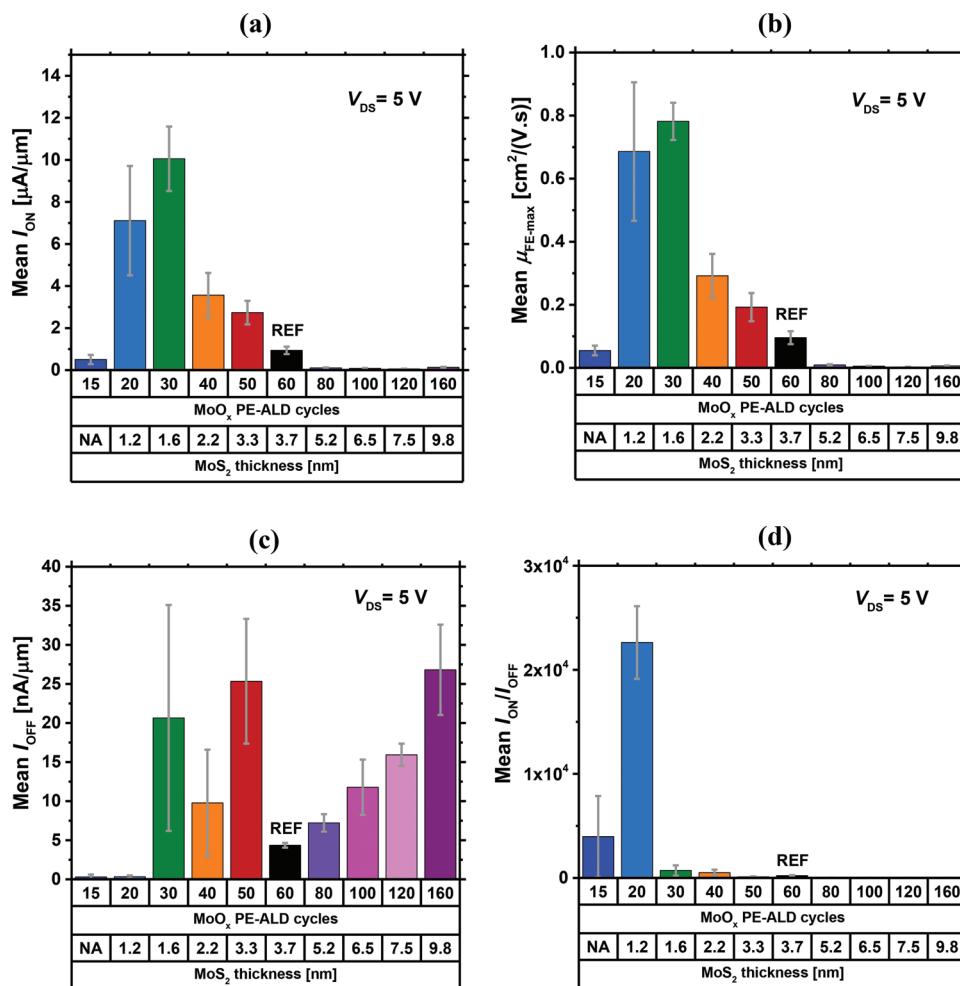
Figure 3. Average statistical data for a) I_{ON}, b) maximum μ_{FE}, c) I_{OFF}, and d) ON/OFF current ratio as a function of initial MoO$_x$ PE-ALD cycles and MoS$_2$ thickness.

(SiO$_2$) capacitance. g_m can be derived from the slope of the transfer curve (at each measured V_{DS}) and C_{ox} from the following equation[58]

$$C_{ox} = (\varepsilon_{SiO_2}\varepsilon_0) / t_{ox}$$

(2)

In Equation (2), ε_{SiO_2} and ε_o are the SiO$_2$ relative dielectric constant and vacuum permittivity, respectively, and t_{ox} is the SiO$_2$ thickness. Similar to the mean I_{ON}, the mean maximum μ_{FE} shows a nonmonotonic trend with varying the channel thickness. As can be seen from Figure 3b, for the devices with only 30 cycles of initial MoO$_x$ (equal to ≈1.6 nm MoS$_2$) the mean maximum μ_{FE} reaches ≈0.8 cm^2 V^{-1} s^{-1}, which is at least eight times more than the reference case. On the other hand, for the devices with thicker MoS$_2$ films, μ_{FE} falls substantially below that of the reference. Such a nonmonotonic trend for μ_{FE} has also been observed previously by Das et al.,[22,23] Li et al.[28] and Lin et al.,[24] in exfoliated-based MoS$_2$ FETs which were not capped by any dielectric layer.

Das et al. have proposed a resistor network model for explaining the observed nonmonotonic behavior of μ_{FE}.[23] Based on their findings, for less than 6 nm of MoS$_2$, μ_{FE}

is mainly degraded by Coulombic scattering. In fact, the screening efficiency against the Coulombic scattering potentials is relatively low in ultrathin MoS$_2$ films of only a few monolayers, and the scattering rates are high,[28] especially if no dielectric capping layer is employed.[14,59–61] For such cases, there are not many outer layers present to shield the bottom MoS$_2$ layers from the interfacial Coulombic scattering sources (e.g., substrate surface dangling bonds, charged impurities and environmental adsorbates). Furthermore, bottom MoS$_2$ layers are considered as the most electrically active layers in back-gate device geometry. As a result, when a few layer MoS$_2$ is not well protected, a degraded device performance can be observed. For more than 12 nm of MoS$_2$, Das et al. highlighted the role of interlayer resistance (R_{int}),[23,62] as the dominating mobility degrading mechanism. Because layers in a multilayer MoS$_2$ are held together by weak vdW interactions, a tunneling barrier is present in between the individual layers. This barrier contributes to the total resistance and negatively influences the carrier transport from the source/drain contacts to the lower layers of MoS$_2$. R_{int} is estimated to be 2.0 kΩ μm between two layers of MoS$_2$.[63] Therefore, Das et al. suggested an optimal thickness window of 6–12 nm of MoS$_2$ for harvesting the most from the

ADVANCED
SCIENCE NEWS
www.advancedsciencenews.com

ADVANCED
ELECTRONIC
MATERIALS
www.advelectronicmat.de

MoS_2-based FETs. This advice is often followed by the research community. However, using the proposed thickness range for our synthetic MoS_2 films led to a highly degraded device electrical behavior, as evidenced from Figure 3a,b.

Based on our analyses, only ≈1.2–1.6 nm of MoS_2 is adequate for achieving the most optimal ON-state performance in our fabricated devices, pin-pointing the principal differences between the exfoliated-based MoS_2 flakes and the synthetic-based counterparts. In addition to the actual dissimilarities between the MoS_2 preparation methods in our study and that of Das et al., it is important to mention that we grew a dielectric capping layer of AlO_x/HfO_x (5/25 nm) on our devices. The dielectric capping layer is well-known for suppressing the Coulombic scattering on/in MoS_2[60] and inducing dopants to the MoS_2 conduction band minimum (E_c),[9,17,64] partially explaining the observed device performance improvements for our relatively thin MoS_2 channels.

Figure 3c statistically illustrates the mean I_{OFF}. Overall, reducing the initial MoO_x number of deposition cycles from 160 to 15 improves I_{OFF} by nearly two orders of magnitude. As can be seen, I_{OFF} drops from 26.8 nA μm^{-1} (for the devices with 160 cycles of initial MoO_x) down to 0.3 nA μm^{-1} (for the devices with both 20 and 15 cycles of initial MoO_x). This is first because by scaling down the MoS_2 thickness, the back-gate electrostatic control over the channel increases. Therefore, the gate can more efficiently deplete the channel in the OFF-state regime, as it has especially better control over the dopants induced by the dielectric capping layer from the top.[65,66] Second, the MoS_2 E_g is known to increase with reducing its number of monolayers, due to quantum confinement effects.[21] As a result, the band edge position of MoS_2 changes with respect to the Ti/Au contact work function, leading to a higher SBH for thinner MoS_2 films.[31] In the OFF-state regime, the carrier injection from the contacts to MoS_2 is mainly governed by thermionic emission from the Schottky barrier[22,67] (which is higher for thinner MoS_2 films[31]) partly explaining the I_{OFF} reduction with reducing the MoS_2 thickness. The OFF-state current dependence on E_g has also been observed previously for ultrathin (≈2 nm) disordered Si channels in thin-film transistors, where I_{OFF} is shown to be related to E_g by an exponentially decaying factor.[68]

Finally, the average ON/OFF current ratios are displayed in Figure 3d. As can be seen, this ratio maximizes only for the devices with 20 cycles of initial MoO_x (equal to ≈1.2 nm MoS_2). For these cases, the ON/OFF current ratio improves two orders of magnitude (as compared with the reference) and reaches more than 2×10^4. Therefore, ≈1.2 nm of MoS_2 is considered as the most optimal channel thickness for our fabricated FETs.

The double sweep transfer curve of the most optimal case is also compared with respect to the reference, as shown in **Figure 4**. In addition to the enhanced device metrics for the ≈1.2 nm thick MoS_2 FETs, the threshold voltage (V_T) shifts to more negative values, implying an increase in the n-type doping concentration of MoS_2 by reducing its thickness (while maintaining the OFF-state current to low values).

The repeatability of the data provided in Figure 3 is worthwhile being investigated as well. Therefore, a second set of MoS_2 FETs from 20, 60, and 80 cycles of initial MoO_x were fabricated and characterized. The obtained values for the device metrics are similar to what is shown in Figure 3 as the first set,
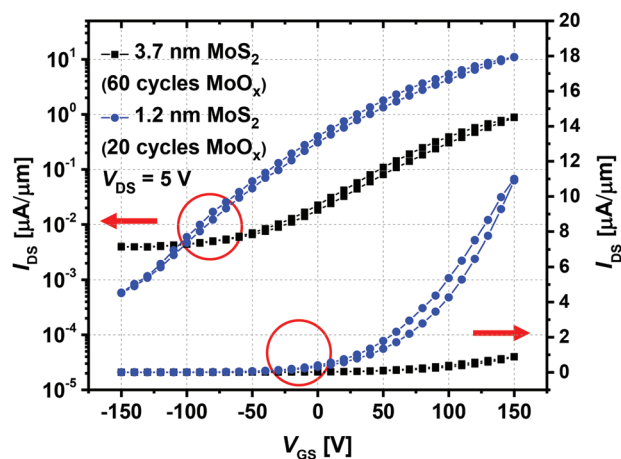

Figure 4. Transfer curves of the MoS_2 FETs with ≈1.2 nm MoS_2 (the most optimal case) and ≈3.7 nm MoS_2 (reference) in both semilog and linear scales.

and the devices with ≈1.2 nm MoS_2 (60 cycles of initial MoO_x) again outperform the reference. See Section S4 in the Supporting Information and the associated discussion.

2.3. STEM Analysis for Ultrathin MoS_2

To further elucidate the observed trends for the devices made from ultrathin MoS_2 channels, the microstructure, morphology, and the surface coverage of such films were evaluated. For this purpose, STEM imaging was performed on the MoS_2 films with 10, 15, and 20 PE-ALD cycles of initial MoO_x.

Figure 5a–c displays high angle annular dark field (HAADF) top view STEM images of the resultant MoS_2 films, for the as-mentioned number of initial MoO_x PE-ALD cycles. Selected area electron diffraction (SAED) patterns, acquired from ≈0.6 μm diameter areas, are also provided as the inset.

In Figure 5a, the MoS_2 film obtained from sulfurizing 10 cycles of PE-ALD MoO_x exhibits quite a uniform and almost continuous surface coverage, with few small pinholes (dark areas). In addition, two closed and continuous rings are observed in the SAED pattern, implying that many nanosized crystals are contributing to the film texture. Both the surface coverage and the film crystallinity are more evident in a higher resolution STEM image, provided in Figure 5d. On average, the grain size does not exceed above 20 nm. This is more clearly shown in Figure S4a,b of the Supporting Information.

On the other hand, the MoS_2 film obtained from sulfurizing 15 cycles of PE-ALD MoO_x demonstrates a percolated network[69] of crystallites, as evidenced in Figure 5b. The detection of brighter rings in the SAED pattern also reveals that the film is more crystalline than the 10-cycle case, although the resultant MoS_2 fails to completely cover the entire SiO_2 substrate. In addition, the concentric rings are less continuous, implying that less grains are present in the selected area, as the average grain size becomes larger for the 15-cycle case than the 10-cycle counterpart. For better visualizing the film morphology, a higher resolution HAADF-STEM image is also provided in Figure 5e. As can be seen, despite the incomplete surface
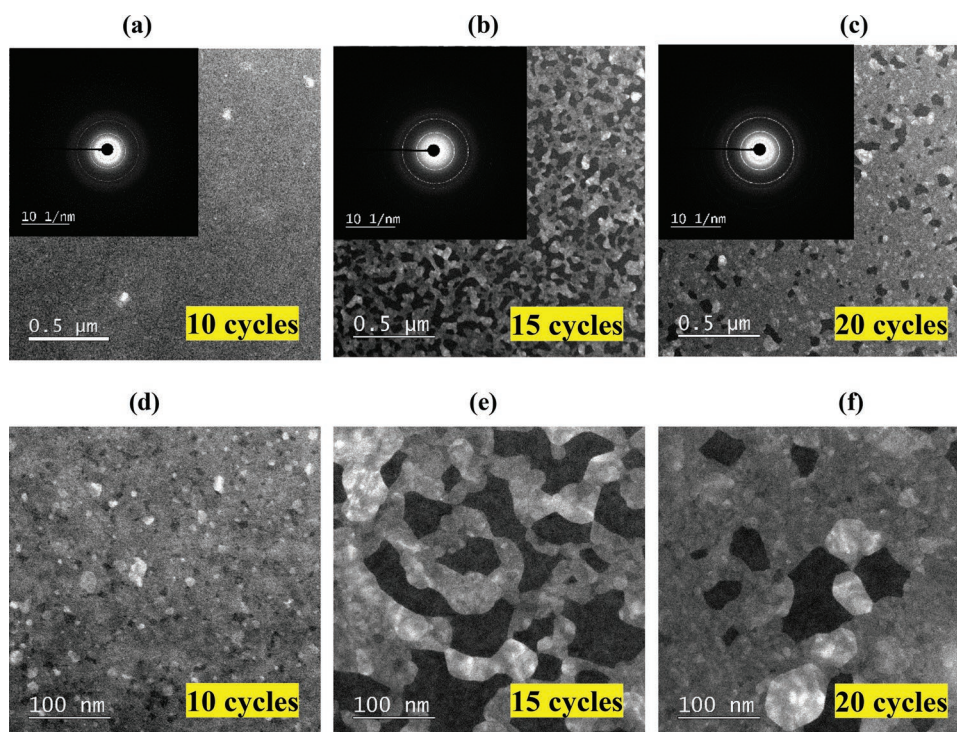
**ADVANCED
SCIENCE NEWS**
www.advancedsciencenews.com

**ADVANCED
ELECTRONIC
MATERIALS**
www.advelectronicmat.de

Figure 5. a–c) STEM images in high angle annular dark field (HAADF) mode for ultrathin MoS_2 films obtained from 10, 15, and 20 cycles of initial PE-ALD MoO_x. The inset of each image corresponds to the selected area electron diffraction pattern (SAED), acquired from ≈0.6 μm diameter areas, (d-f) are higher magnification mode HAADF-STEM images for the as-mentioned cases.

coverage, the grain domains are still connected. In addition, the average grain size slightly increases compared with the 10-cycle case. The latter is more clearly displayed in Figure S4c,d of the Supporting Information.

Considering the MoS_2 film obtained from sulfurizing 20 cycles of PE-ALD MoO_x (Figure 5c,f), the polycrystalline network expands further than the 15-cycle case. The fraction of dark areas on the substrate also reduces while the grain domains still maintain their connection. See Figure S4e,f in the Supporting Information for higher magnification STEM images. Moreover, the average grain size increases, as apparent from the discontinuous nature of the rings in the SAED pattern. With further increasing the number of initial MoO_x deposition cycles to 60, a fully closed and polycrystalline MoS_2 film can be achieved upon the sulfurization process, where grain domains expand to an average size of 70 nm. The 60-cycle case is not shown here, as it has already been studied in our previous work.[45] We do also take note that before the sulfurization process, the initial PE-ALD MoO_x films (grown at 50 °C) are all amorphous and fully/uniformly cover the SiO_2 substrates.[70]

In addition to the HAADF-STEM images, the STEM-energy dispersive X-ray (EDX) elemental mappings of Mo and S are provided in **Figure 6**. The analysis confirms that the MoS_2 layer formed after sulfurizing 10 cycles of PE-ALD MoO_x covers the SiO_2 substrate quite homogeneously and has only few pinholes. By increasing the number of MoO_x deposition cycles to 15 and 20, the surface coverage of the final MoS_2 film initially reduces then increases again. The elemental mappings of the 15- and 20-cycle cases also verify that the dark areas in the images are empty spots with no Mo or S, above the EDX detection limit.

This is further elucidated in the Supporting Information. See Figure S5 in the Supporting Information and the associated discussion.

To elaborate the STEM observations, one can realize few transitions with regards to the MoS_2 film texture. By sequentially increasing the number of initial MoO_x PE-ALD cycles, first, a homogeneous ultrathin MoS_2 film of nanosized crystals (10-cycle case) then, a percolated network of crystallites (15- and 20-cycle cases) and finally, a fully closed polycrystalline MoS_2 film (60-cycle case) is achieved upon the sulfurization process. To clarify the observed texture evolution, we hypothesize that the two following mechanisms can concurrently take place when the PE-ALD grown MoO_x films are exposed to H_2S gas at elevated temperatures: MoO_x sublimation[54] and MoO_x sulfurization.[50] The former is known to start at temperatures above 470 °C.[54]

For ultrathin layers of MoO_x (10-cycle case which leads to a monolayer MoS_2[45]), all the Mo atoms are situated on the substrate surface. Therefore, it is presumed that the entire MoO_x film reacts with H_2S and sulfurizes, leading to an almost continuous, polycrystalline and ultrathin MoS_2 film with few small pinholes. The noted pinholes are most likely originating from the minor MoO_x sublimation during the synthesis process.[54] For thicker MoO_x films (15- and 20-cycle cases), not all the Mo atoms reside on the substrate surface any longer, and H_2S gas needs to diffuse through the inner layers and react with them.[50] Therefore, in the beginning of the process, only the top layer MoO_x sulfurizes. The underlying MoO_x, which is not directly exposed to H_2S, partly sublimates and leaves through the sulfurized top surface. This causes the film to break up and
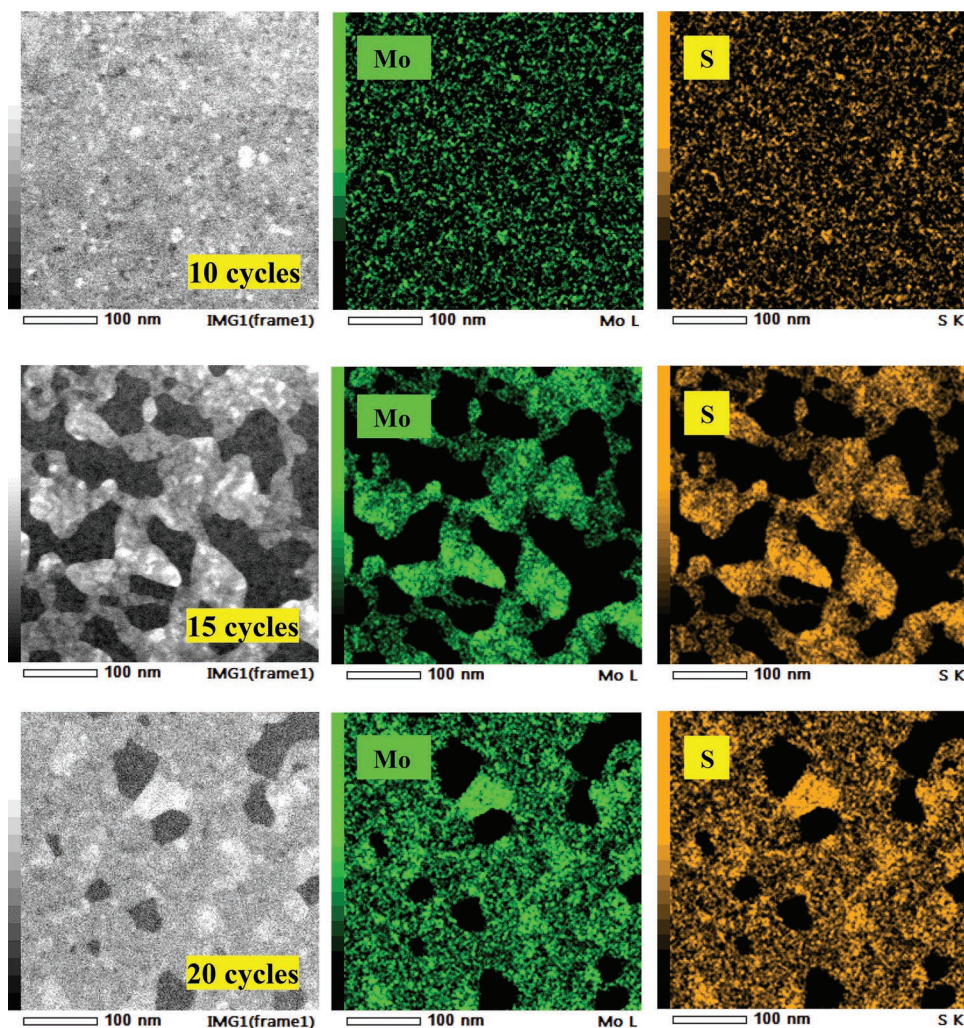
Figure 6. Mo and S elemental mappings, obtained from energy dispersive X-ray spectroscopy (EDX)-STEM imaging, for 10-, 15-, and 20-cycle cases. Black regions denoting voids with no MoS_2.

form the observed percolated network. For the 60-cycle case, the MoO_x sublimation rate is most likely not high enough to result in the film dewetting, and sulfurization is dominating. Therefore, as reported in our previous work,[45] a closed MoS_2 film is achieved.

The STEM imaging assessments bring our attention to several notable points with regards to the electrical performance of our ultrathin MoS_2 FETs. In the MoS_2 films obtained from sulfurizing 10 PE-ALD cycles of MoO_x, many nanosized crystals are contributing to the texture (Figure 5a-inset,d). However, the grain domain sizes are maximum 20 nm (Figure S4a,b, Supporting Information). This explains our failure in demonstrating a working FET for the 10-cycle case, as the MoS_2 films with only 20 nm crystalline domains are generally highly resistive. After sulfurizing 15 PE-ALD cycles of MoO_x, a percolated MoS_2 network with slightly bigger crystalline domains than the 10-cycle case is obtained (Figure 5b,e), which are well-connected (Figure S4c,d, Supporting Information). A working FET could be demonstrated. However, the device metrics are not as intriguing as to when the initial MoO_x PE-ALD cycles increase to 20 (Figure 3a–d), pinpointing the importance of

MoS_2 surface coverage at least up to some extent (Figure 5c,f) as well as the expansion of grain domains for attaining a decent device performance.

The MoS_2 films obtained from sulfurizing 20 PE-ALD cycles of MoO_x led to the most optimal device electrical performance (lowest achieved I_{OFF} and second-best I_{ON}) among all the studied cases. However, such ultrathin MoS_2 films are polycrystalline and not continuous. It is presumed that in addition to the grain size increase, formation of side contacts to MoS_2 from the film discontinuous regions (during the metallization step of the device processing) plays a role in the observed device electrical improvements. A combination of side and top contact geometry is known to improve the overall electrical performance of the MoS_2 FETs.[71–74] In the case of MoS_2 obtained from 20 PE-ALD cycles of MoO_x, we benefit from the open empty areas in the polycrystalline network. These spots seem to serve as locations for the formation of side contacts (in addition to the top contacts) once Ti/Au is evaporated. Therefore, compared to our reference case (with ≈3.7 nm thick MoS_2) the ON-state device metrics improve substantially when ≈1.2 nm MoS_2 (20 cycles of initial MoO_x) is employed as the channel.

ADVANCED
SCIENCE NEWS
www.advancedsciencenews.com

ADVANCED
ELECTRONIC
MATERIALS
www.advelectronicmat.de

Altogether, the electrical properties of synthetic-based MoS_2 FETs demonstrate a strong dependence on the MoS_2 film morphology (parallel to the MoS_2 thickness) which should not be underestimated when analyzing the $I–V$ results. Unlike the exfoliated counterparts, only $\approx$1.2 nm of MoS_2 is sufficient for obtaining the most optimal device electrical performance.

3. Conclusions

To conclude, our work shows that with varying the PE-ALD cycles of MoO_x, the final MoS_2 film thickness can be precisely controlled, and the electrical properties of the fabricated MoS_2 FETs can be tuned. By reducing the MoS_2 thickness down to $\approx$1.2 nm (reducing the PE-ALD cycles of MoO_x down to 20) the device metrics improve substantially. From the electrical standpoint, these observed improvements are partly associated with the higher degree of gate electrostatic control over thinner MoS_2 channels, which specifically manifests itself in the device OFF-state regime. An in-depth analysis of the film microstructure provides further insights into the electrical observations and reveals that the thickness dependent electrical properties of the fabricated MoS_2 FETs are also highly governed by a morphological effect. Utilization of only $\approx$1.2 nm MoS_2 leads to the best device electrical performance. Such ultrathin synthesized MoS_2 films are shown to be discontinuous. The discontinuous nature of ultrathin MoS_2 can allow for side contact formation once the metallic contacts are evaporated, partly explaining the observed ON-state improvements in the device figures of merit. Our findings highlight that an independent re-evaluation of the optimum channel thickness for the synthetic-based MoS_2 FETs is always required, due to the principal differences between the exfoliated MoS_2 and its synthetic counterparts. In addition, the role of MoS_2 film morphology should not be overlooked.

4. Experimental Section

MoS_2 Synthesis: The MoS_2 films were synthesized by a two-step approach, whereby large-area MoO_x films of various thicknesses (deposition cycles) were initially deposited using PE-ALD,[70] in an Oxford instruments ALD reactor (FlexAl) at 50 °C, on highly doped (p^{++}) Si substrates which were thermally coated with $\approx$285 nm SiO_2. The as-deposited MoO_x films were then sulfurized in H_2S/Ar (10%/90%) atmosphere at 900 °C for 45 min, in a home-built tube furnace. The entire details of the film synthesis conditions and other specifications, such as the film morphology, thickness and interlayer spacing (measured by AFM and cross-sectional STEM respectively) as well as photoluminescence data for ultrathin layers of MoS_2 are reported in a previous study.[45]

Film Thickness Measurement: During the PE-ALD of MoO_x, in situ SE (J.A. Woollam Co., Inc. M-2000FI, 0.75–5 eV) was performed, to measure the film thickness and the GPC. After the sulfurization process, the obtained MoS_2 film thicknesses were once more inspected by ex situ SE (J.A. Woollam Co., Inc. M-2000D, 1.25–6.5 eV). The collected data for both in situ MoO_x and ex situ MoS_2 SE measurements were analyzed with Complete EASE software and its embedded fitting models (Cauchy for MoO_x and B-spline for MoS_2). It was noted that the thickness data obtained by the SE measurements are reasonably in accordance with the results from the AFM measurements that are already reported in the previous work.[45] The AFM line-profile of the ultrathin MoS_2 films

are also provided in Figure S1 in the Supporting Information, for further confirmation.

General MoS_2 Film Inspections: The quality of the as-synthesized MoS_2 films of various thicknesses was inspected using Raman and XPS analyses. The setup used for the Raman analysis was Renishaw InVia confocal Raman microscope, equipped with a 514 nm laser, an integrated switchable grating of 600 or 1800 lines mm^{-1} and a charge coupled device detector. During the Raman scans, five accumulations with an acquisition time of 10 s were taken, using a laser power of < 0.2 mW focused on a $\approx$1 µm region. For the XPS analysis, Thermo Scientific K-alpha KA1066 spectrometer (Thermo Fisher Scientific, Waltham, MA) with a monochromatic Al Kα X-ray radiation source ($h\nu$ = 1486.6 eV) was utilized. An X-ray beam spot size of 400 µm, at a take-off angle of 60° and a pass energy of 50 eV were selected for the measurements. An electron flood gun was also used for correcting the nonuniform and differential charging on the samples. The acquired spectra were chemically quantified and deconvoluted with Avantage software. All the peak binding energies were calibrated with respect to the C 1s adventitious carbon peak (284.8 eV).

Fabrication of MoS_2 FETs: Back-gate FETs were fabricated for series of MoS_2 thicknesses using standard electron beam lithography (EBL). An organic resist (poly(methyl methacrylate) (PMMA) A4, 950 K) was initially spin-coated on MoS_2 films for 60 s, with a spin speed of 4000 rpm and eventually baked on a hot plate for 5 min at 180 °C. EBL was then employed for defining the contact windows using RAITH micrograph (EBPG 5150), followed by a development step in a resist developer solution (methyl isobutyl ketone/isopropyl alcohol, [1:3] ratio) to dissolve/open the exposed regions. Next, 5/95 nm of Ti/Au was evaporated using an e-beam evaporator at room temperature, with a deposition rate of 1 Å s^{-1} and a base pressure of $\approx 4 \times 10^{-7}$ mbar (near ultrahigh vacuum). Based on a previous work,[57] 5/95 nm of Ti/Au is found to be the most optimal thickness combination for the contacts to the ALD-based MoS_2. After metallization, a standard lift-off process was pursued for contact delineation. This was done by overnight submerging the samples into acetone and subsequently removing the Ti/Au together with PMMA from the unexposed areas. For defining the channel regions and isolating the individual device blocks, a second EBL patterning/development was required. These steps were followed by dry etching the MoS_2 with SF_6/O_2 plasma gas mixture of 16/4 sccm flow rates for 20 s, at room-temperature and a pressure of 22.5 mTorr, with a forward power of 25 W, in an Oxford Instruments Reactive Ion Etching reactor. The PMMA was then completely removed by soaking the samples again into acetone. Finally, the fabricated devices were capped with 5/25 nm of thermal ALD AlO_x[75]/PE-ALD HfO_x,[76] grown at 100 °C (in the FlexAl reactor).

Electrical Characterization: The electrical performance of the back-gate MoS_2 FETs with different channel thicknesses was evaluated on a 500 nm long and 1 µm wide channel dimensions. The current voltage ($I–V$) measurements were performed in a cryogenic probe station (Janis ST-500) at room temperature and a base pressure of $\approx 1.9 \times 10^{-4}$ mbar, connected to a Keithley 4200-semiconductor characterization system parameter analyzer.

Structural Characterization: The microstructure, morphology, and surface coverage of the MoS_2 films were evaluated by STEM imaging. For this purpose, a JEOL atomic resolution microscope 200 F operated at 200 kV and equipped with a 100 mm^2 Centurio silicon drift detector EDX spectroscopy detector was employed. Electron transparent SiN_x TEM windows coated with $\approx$5 nm ALD SiO_2 were used as the imaging substrates, on which various MoS_2 thicknesses were grown with a similar synthesis method as mentioned above.

Supporting Information

Supporting Information is available from the Wiley Online Library or from the author.

Conflict of Interest

The authors declare no conflict of interest.

Data Availability Statement

The data that support the findings of this study are available from the corresponding author upon reasonable request.

[1] A. K. Geim, I. V. Grigorieva, *Nature* **2013**, *499*, 419.

[2] S. Manzeli, D. Ovchinnikov, D. Pasquier, O. V. Yazyev, A. Kis, *Nat. Rev. Mater.* **2017**, *2*, 17033.

[3] C. D. English, K. K. H. Smithe, R. L. Xu, E. Pop, in *Tech. Dig. – Int. Electron Devices Meet. IEDM*, IEEE, Piscataway, NJ **2017**, pp. 5.6.1–5.6.4.

[4] K. Alam, R. K. Lake, *IEEE Trans. Electron Devices* **2012**, *59*, 3250.

[5] D. Akinwande, C. Huyghebaert, C.-H. Wang, M. I. Serna, S. Goossens, L.-J. Li, H.-S. P. Wong, F. H. L. Koppens, *Nature* **2019**, *573*, 507.

[6] C. Huyghebaert, T. Schram, Q. Smets, T. K. Agarwal, D. Verreck, S. Brems, A. Phommahaxay, D. Chiappe, S. El Kazzi, C. Lockhart de la Rosa, G. Arutchelvan, D. Cott, J. Ludwig, A. Gaur, S. Sutar, A. Leonhardt, D. Marinov, D. Lin, M. Caymax, I. Asselberghs, G. Pourtois, I. P. Radu, in *2018 IEEE Int. Electron Devices Meet*, IEEE, Piscataway, NJ **2018**, pp. 22.1.1–22.1.4.

[7] R. Ganatra, Q. Zhang, *ACS Nano* **2014**, *8*, 4074.

[8] Q. H. Wang, K. Kalantar-Zadeh, A. Kis, J. N. Coleman, M. S. Strano, *Nat. Nanotechnol.* **2012**, *7*, 699.

[9] C. J. McClellan, E. Yalon, K. K. H. Smithe, S. V. Suryavanshi, E. Pop, *ACS Nano* **2021**, *15*, 1587.

[10] Y. Liu, J. Guo, Y. Wu, E. Zhu, N. O. Weiss, Q. He, H. Wu, H. C. Cheng, Y. Xu, I. Shakir, Y. Huang, X. Duan, *Nano Lett.* **2016**, *16*, 6337.

[11] P.-C. Shen, C. Su, Y. Lin, A.-S. Chou, C.-C. Cheng, J.-H. Park, M.-H. Chiu, A.-Y. Lu, H.-L. Tang, M. M. Tavakoli, G. Pitner, X. Ji, Z. Cai, N. Mao, J. Wang, V. Tung, J. Li, J. Bokor, A. Zettl, C.-I. Wu, T. Palacios, L.-J. Li, J. Kong, *Nature* **2021**, *593*, 211.

[12] W. Li, J. Zhou, S. Cai, Z. Yu, J. Zhang, N. Fang, T. Li, Y. Wu, T. Chen, X. Xie, H. Ma, K. Yan, N. Dai, X. Wu, H. Zhao, Z. Wang, D. He, L. Pan, Y. Shi, P. Wang, W. Chen, K. Nagashio, X. Duan, X. Wang, *Nat. Electron.* **2019**, *2*, 563.

[13] P. Bolshakov, C. M. Smyth, A. Khosravi, P. Zhao, P. K. Hurley, C. L. Hinkle, R. M. Wallace, C. D. Young, *ACS Appl. Electron. Mater.* **2019**, *1*, 210.

[14] B. Radisavljevic, A. Radenovic, J. Brivio, V. Giacometti, A. Kis, *Nat. Nanotechnol.* **2011**, *6*, 147.

[15] S. Kim, A. Konar, W.-S. Hwang, J. H. Lee, J. Lee, J. Yang, C. Jung, H. Kim, J.-B. Yoo, J.-Y. Choi, Y. W. Jin, S. Y. Lee, D. Jena, W. Choi, K. Kim, *Nat. Commun.* **2012**, *3*, 1011.

[16] Y. Y. Illarionov, K. K. H. Smithe, M. Waltl, T. Knobloch, E. Pop, T. Grasser, *IEEE Electron Device Lett.* **2017**, *38*, 1763.

[17] A. Leonhardt, D. Chiappe, V. V. Afanas'ev, S. El Kazzi, I. Shlyakhov, T. Conard, A. Franquet, C. Huyghebaert, S. de Gendt, *ACS Appl. Mater. Interfaces* **2019**, *11*, 42697.

[18] K. K. H. Smithe, S. V. Suryavanshi, M. Muñoz Rojo, A. D. Tedjarati, E. Pop, *ACS Nano* **2017**, *11*, 8456.

[19] K. F. Mak, C. Lee, J. Hone, J. Shan, T. F. Heinz, *Phys. Rev. Lett.* **2010**, *105*, 136805.

[20] A. Splendiani, L. Sun, Y. Zhang, T. Li, J. Kim, C.-Y. Chim, G. Galli, F. Wang, *Nano Lett.* **2010**, *10*, 1271.

[21] A. Kuc, N. Zibouche, T. Heine, *Phys. Rev. B* **2011**, *83*, 245213.

[22] S. Das, H.-Y. Chen, A. V. Penumatcha, J. Appenzeller, *Nano Lett.* **2013**, *13*, 100.

[23] S. Das, J. Appenzeller, *Phys. Status Solidi RRL* **2013**, *7*, 268.

[24] M.-W. Lin, I. I. Kravchenko, J. Fowlkes, X. Li, A. A. Puretzky, C. M. Rouleau, D. B. Geohegan, K. Xiao, *Nanotechnology* **2016**, *27*, 165203.

[25] X. Cui, G.-H. Lee, Y. D. Kim, G. Arefe, P. Y. Huang, C.-H. Lee, D. A. Chenet, X. Zhang, L. Wang, F. Ye, F. Pizzocchero, B. S. Jessen, K. Watanabe, T. Taniguchi, D. A. Muller, T. Low, P. Kim, J. Hone, *Nat. Nanotechnol.* **2015**, *10*, 534.

[26] J. H. Kim, T. H. Kim, H. Lee, Y. R. Park, W. Choi, C. J. Lee, *AIP Adv.* **2016**, *6*, 065106.

[27] S.-W. Min, H. S. Lee, H. J. Choi, M. K. Park, T. Nam, H. Kim, S. Ryu, S. Im, *Nanoscale* **2013**, *5*, 548.

[28] S.-L. Li, K. Wakabayashi, Y. Xu, S. Nakaharai, K. Komatsu, W.-W. Li, Y.-F. Lin, A. Aparecido-Ferreira, K. Tsukagoshi, *Nano Lett.* **2013**, *13*, 3546.

[29] M. Kayyalha, J. Maassen, M. Lundstrom, L. Shi, Y. P. Chen, *J. Appl. Phys.* **2016**, *120*, 134305.

[30] M. D. Siao, W. C. Shen, R. S. Chen, Z. W. Chang, M. C. Shih, Y. P. Chiu, C.-M. Cheng, *Nat. Commun.* **2018**, *9*, 1442.

[31] S.-L. Li, K. Komatsu, S. Nakaharai, Y.-F. Lin, M. Yamamoto, X. Duan, K. Tsukagoshi, *ACS Nano* **2014**, *8*, 12836.

[32] K. Kang, S. Xie, L. Huang, Y. Han, P. Y. Huang, K. F. Mak, C.-J. Kim, D. Muller, J. Park, *Nature* **2015**, *520*, 656.

[33] H. Ago, in *2020 Int. Symp. VLSI Technol. Syst. Appl.* IEEE, Piscataway, NJ **2020**, p. 139.

[34] Y.-H. Lee, X.-Q. Zhang, W. Zhang, M.-T. Chang, C.-T. Lin, K.-D. Chang, Y.-C. Yu, J. T.-W. Wang, C.-S. Chang, L.-J. Li, T.-W. Lin, *Adv. Mater.* **2012**, *24*, 2320.

[35] D. Chiappe, J. Ludwig, A. Leonhardt, S. El Kazzi, A. Nalin Mehta, T. Nuytten, U. Celano, S. Sutar, G. Pourtois, M. Caymax, K. Paredis, W. Vandervorst, D. Lin, S. De Gendt, K. Barla, C. Huyghebaert, I. Asselberghs, I. Radu, *Nanotechnology* **2018**, *29*, 425602.

[36] T. Kim, J. Mun, H. Park, D. Joung, M. Diware, C. Won, J. Park, S.-H. Jeong, S.-W. Kang, *Nanotechnology* **2017**, *28*, 18LT01.

[37] Y. Zhan, Z. Liu, S. Najmaei, P. M. Ajayan, J. Lou, *Small* **2012**, *8*, 966.

[38] D. Marinov, J.-F. de Marneffe, Q. Smets, G. Arutchelvan, K. M. Bal, E. Voronina, T. Rakhimova, Y. Mankelevich, S. El Kazzi, A. Nalin Mehta, P.-J. Wyndaele, M. H. Heyne, J. Zhang, P. C. With,

S. Banerjee, E. C. Neyts, I. Asselberghs, D. Lin, S. De Gendt, *npj 2D Mater. Appl.* **2021**, *5*, 17.

[39] V. V. Afanas'ev, D. Chiappe, M. Perucchini, M. Houssa, C. Huyghebaert, I. Radu, A. Stesmans, *Nanotechnology* **2019**, *30*, 055702.

[40] A. Sharma, M. A. Verheijen, L. Wu, S. Karwal, V. Vandalon, H. C. M. Knoops, R. S. Sundaram, J. P. Hofmann, W. M. M. (Erwin) Kessels, A. A. Bol, *Nanoscale* **2018**, *10*, 8615.

[41] Z.-L. Tian, D.-H. Zhao, H. Liu, H. Zhu, L. Chen, Q.-Q. Sun, D. W. Zhang, *ACS Appl. Nano Mater.* **2019**, *2*, 7810.

[42] W. Jeon, Y. Cho, S. Jo, J. H. Ahn, S. J. Jeong, *Adv. Mater.* **2017**, *29*, 1703031.

[43] J. J. Pyeon, I.-H. Baek, W. C. Lim, K. H. Chae, S. H. Han, G. Y. Lee, S.-H. Baek, J.-S. Kim, J.-W. Choi, T.-M. Chung, J. H. Han, C.-Y. Kang, S. K. Kim, *Nanoscale* **2018**, *10*, 17712.

[44] J.-G. Song, J. Park, W. Lee, T. Choi, H. Jung, C. W. Lee, S.-H. Hwang, J. M. Myoung, J.-H. Jung, S.-H. Kim, C. Lansalot-Matras, H. Kim, *ACS Nano* **2013**, *7*, 11333.

[45] A. Sharma, R. Mahlouji, L. Wu, M. A. Verheijen, V. Vandalon, S. Balasubramanyam, J. P. Hofmann, W. M. M. (Erwin) Kessels, A. A. Bol, *Nanotechnology* **2020**, *31*, 255603.

[46] S. M. George, *Chem. Rev.* **2010**, *110*, 111.

[47] H. B. Profijt, S. E. Potts, M. C. M. van de Sanden, W. M. M. Kessels, *J. Vac. Sci. Technol. A* **2011**, *29*, 050801.

[48] A. M. van der Zande, P. Y. Huang, D. A. Chenet, T. C. Berkelbach, Y. You, G.-H. Lee, T. F. Heinz, D. R. Reichman, D. A. Muller, J. C. Hone, *Nat. Mater.* **2013**, *12*, 554.

[49] J. Hong, Z. Hu, M. Probert, K. Li, D. Lv, X. Yang, L. Gu, N. Mao, Q. Feng, L. Xie, J. Zhang, D. Wu, Z. Zhang, C. Jin, W. Ji, X. Zhang, J. Yuan, Z. Zhang, *Nat. Commun.* **2015**, *6*, 6293.

[50] M. H. Heyne, D. Chiappe, J. Meersschaut, T. Nuytten, T. Conard, H. Bender, C. Huyghebaert, I. P. Radu, M. Caymax, J.-F. de Marneffe, E. C. Neyts, S. De Gendt, *J. Mater. Chem. C* **2016**, *4*, 1295.

[51] D. Chiappe, I. Asselberghs, S. Sutar, S. Iacovo, V. Afanas'ev, A. Stesmans, Y. Balaji, L. Peters, M. Heyne, M. Mannarino, W. Vandervorst, S. Sayan, C. Huyghebaert, M. Caymax, M. Heyns, S. De Gendt, I. Radu, A. Thean, *Adv. Mater. Interfaces* **2016**, *3*, 1500635.

[52] S. Zhang, H. Xu, F. Liao, Y. Sun, K. Ba, Z. Sun, Z.-J. Qiu, Z. Xu, H. Zhu, L. Chen, Q. Sun, P. Zhou, W. Bao, D. W. Zhang, *Nanotechnology* **2019**, *30*, 174002.

[53] S. Hussain, M. A. Shehzad, D. Vikraman, M. F. Khan, J. Singh, D.-C. Choi, Y. Seo, J. Eom, W.-G. Lee, J. Jung, *Nanoscale* **2016**, *8*, 4340.

[54] R. Szoszkiewicz, M. Rogala, P. Dabrowski, *Materials (Basel)* **2020**, *13*, 3067.

[55] C. Lee, H. Yan, L. E. Brus, T. F. Heinz, J. Hone, S. Ryu, *ACS Nano* **2010**, *4*, 2695.

[56] I. S. Kim, V. K. Sangwan, D. Jariwala, J. D. Wood, S. Park, K.-S. Chen, F. Shi, F. Ruiz-Zepeda, A. Ponce, M. Jose-Yacaman, V. P. Dravid, T. J. Marks, M. C. Hersam, L. J. Lauhon, *ACS Nano* **2014**, *8*, 10551.

[57] R. Mahlouji, Y. Zhang, M. A. Verheijen, J. P. Hofmann, W. M. M. Kessels, A. A. Sagade, A. A. Bol, *ACS Appl. Electron. Mater.* **2021**, *3*, 3185.

[58] D. K. Schroder, *Semiconductor Material and Device Characterization*, John Wiley and Sons, Inc., Hoboken, NJ **2005**.

[59] D. Jena, A. Konar, *Phys. Rev. Lett.* **2007**, *98*, 136805.

[60] N. Ma, D. Jena, *Phys. Rev. X* **2014**, *4*, 011043.

[61] K. Kaasbjerg, K. S. Thygesen, K. W. Jacobsen, *Phys. Rev. B: Condens. Matter Mater. Phys.* **2012**, *85*, 115317.

[62] S. Das, J. Appenzeller, *Nano Lett.* **2013**, *13*, 3396.

[63] J. Na, M. Shin, M.-K. Joo, J. Huh, Y. Jeong Kim, H. Jong Choi, J. Hyung Shim, G.-T. Kim, *Appl. Phys. Lett.* **2014**, *104*, 233502.

[64] A. Valsaraj, J. Chang, A. Rai, L. F. Register, S. K. Banerjee, *2D Mater.* **2015**, *2*, 045009.

[65] Y. Yoon, K. Ganapathi, S. Salahuddin, *Nano Lett.* **2011**, *11*, 3768.

[66] C. J. Lockhart de la Rosa, G. Arutchelvan, A. Leonhardt, C. Huyghebaert, I. Radu, M. Heyns, S. De Gendt, *APL Mater.* **2018**, *6*, 058301.

[67] J. Appenzeller, F. Zhang, S. Das, J. Knoch, in *2D Mater. Nanoelectron*, Taylor and Francis Group, LLC, Boca Raton, FL **2016**, pp. 207–240.

[68] X. Guo, T. Ishii, S. R. P. Silva, *IEEE Electron Device Lett.* **2008**, *29*, 588.

[69] X. Gao, J. Yin, G. Bian, H. Y. Liu, C. P. Wang, X. X. Pang, J. Zhu, *Nano Res.* **2020**, 2255.

[70] M. F. J. Vos, B. Macco, N. F. W. Thissen, A. A. Bol, W. M. M. (Erwin) Kessels, *J. Vac. Sci. Technol., A* **2016**, *34*, 01A103.

[71] J. Kang, W. Liu, D. Sarkar, D. Jena, K. Banerjee, *Phys. Rev. X* **2014**, *4*, 031005.

[72] L. Wang, I. Meric, P. Y. Huang, Q. Gao, Y. Gao, H. Tran, T. Taniguchi, K. Watanabe, L. M. Campos, D. A. Muller, J. Guo, P. Kim, J. Hone, K. L. Shepard, C. R. Dean, *Science* **2013**, *342*, 614.

[73] M. H. D. Guimarães, H. Gao, Y. Han, K. Kang, S. Xie, C.-J. Kim, D. A. Muller, D. C. Ralph, J. Park, *ACS Nano* **2016**, *10*, 6392.

[74] K. Parto, A. Pal, T. Chavan, K. Agashiwala, C.-H. Yeh, W. Cao, K. Banerjee, *Phys. Rev. Appl.* **2021**, *15*, 064068.

[75] K. B. Jinesh, J. L. van Hemmen, M. C. M. van de Sanden, F. Roozeboom, J. H. Klootwijk, W. F. A. Besling, W. M. M. Kessels, *J. Electrochem. Soc.* **2011**, *158*, G21.

[76] A. Sharma, V. Longo, M. A. Verheijen, A. A. Bol, W. M. M. (Erwin) Kessels, *J. Vac. Sci. Technol., A* **2017**, *35*, 01B130.